

## Research Article

# Numerical Investigations on Unsteady Features of Rounded Trailing Edge Airfoils

Bowen Shu <sup>1,2</sup>, Zhenghong Gao <sup>1</sup>, Lin Zhou,<sup>1</sup> and Shusheng Chen <sup>1,3</sup>

<sup>1</sup>School of Aeronautics, Northwestern Polytechnical University, Xi'an 710072, China

<sup>2</sup>Aerospace Technology Institute, China Aerodynamics Research and Development Center, Mianyang 621000, China

<sup>3</sup>AVIC The First Aircraft Institute, Xi'an 710089, China

Correspondence should be addressed to Shusheng Chen; [sshengchen@nwpu.edu.cn](mailto:sshengchen@nwpu.edu.cn)

Received 5 March 2022; Revised 12 September 2022; Accepted 14 November 2022; Published 28 December 2022

Academic Editor: Jinyang Xu

Copyright © 2022 Bowen Shu et al. This is an open access article distributed under the Creative Commons Attribution License, which permits unrestricted use, distribution, and reproduction in any medium, provided the original work is properly cited.

As a practical rounded trailing edge airfoil for coaxial rotors, DBLN-526 is a fore and aft symmetrical airfoil with two steps on its lower side. This airfoil has been used at the inboard section of the coaxial rotor system. As there are always two eddies behind the airfoil because of its rounded trailing edge, the interaction between the separation and transition should be considered. Thus, the unsteady Reynolds-averaged Navier-Stokes- (RANS-) based  $\gamma - \overline{Re}_{\theta t}$  model was used to analyze the unsteady transition and separation features. Three different rounded trailing-edge airfoils were compared with DBLN-526. Power spectrum density analysis and  $\Delta Cl$  calculations demonstrated that the lift coefficient fluctuation of DBLN-526 was smaller than that of other rounded airfoils with different angles. Further investigation indicated that the locations of transition for DBLN-526 can be fixed at a wide range of angles by the unique design on its lower side. Because of this settled transition location, the size of separation is decreased, and the position of separation is settled as well, which leads to a lower lift coefficient fluctuation. The turbulent kinetic energy after the transition was higher, which injected a lot of energy into the boundary layer, and the separation zone near the transition position was relatively smaller. This study provides an indication for controlling separation and reducing unsteady fluctuations for rounded trailing edge airfoils.

## 1. Introduction

Achieving high-speed capability without compromising the hover efficiency has been a challenge for rotary-wing aircrafts. Blade stall on the retreating blade and compressibility effects on the advancing blade are the two main phenomena that limit the maximum speed of a traditional single main rotor aircraft. Coaxial rotor systems can overcome these limitations and enable high speed in vehicles. A coaxial rigid rotor helicopter has been proposed as a future high-performance rotorcraft concept [1]. However, the unsteady loads for the coaxial rotor are at least one order of magnitude larger than those of a single isolated rotor under the same conditions [2, 3]. There are multiple reasons for high vibratory loads, including the interaction between the upper and lower rotors [2, 4, 5] and flow separation in the reverse region [5–7]. Reverse flow occurs when a fluid travels from the geometric trailing edge of an airfoil to the geometric leading edge. The resulting flow

field is generally characterized by a negative lift, early onset of flow separation, and periodic vortex shedding, which is believed to contribute to the unsteady aerodynamic loads experienced by a rotor blade [6]. A recent experimental study on a full-scale UH-60A rotor confirmed that reverse flow was responsible for large unsteady loads [8].

In the 1970s, an investigation was conducted in the Langley low-turbulence pressure tunnel to determine the low-speed two-dimensional characteristics of airfoils (cambered with both leading and rounded trailing edges) to study the aerodynamic characteristics of rounded trailing edge airfoils in reverse flow [9]. The X2 technology demonstrator adopted a rounded trailing edge airfoil DBLN-526 in the inboard section to alleviate flow separation in reverse flow, and the aerodynamic efficiency of the improved XH-59A rotor with rounded trailing airfoils was higher than that of the reference rotor [10, 11]. An experimental investigation of reverse flow over sharp and rounded trailing edge airfoils

was conducted to provide fundamental insight into the selection of airfoils for the inboard section of a rotor blade for optimal performance in both forward and reverse flows [12, 13]. Different experiments indicated that rounded trailing edge airfoils have better performance than traditional sharp trailing edge airfoils [10–13]. The former can reduce drag, weaken flow separation, and delay stall in reverse flow. Although many experimental studies have confirmed the advantages of rounded trailing edge airfoils, only a few numerical studies have focused on them. Sun et al. [14] studied the performance of a 16%-thick rounded trailing edge airfoil, Zhou et al. [15] recently discussed the aerodynamic behavior of rounded trailing edge airfoils at high angles of attack, and Han et al. [16] optimized rounded trailing edge airfoils of different thicknesses. Because the superiority of a rounded trailing edge airfoil over a sharp trailing edge airfoil has been proven in previous experimental research, it is important to explore the unsteady aerodynamic characteristics of rounded trailing edge airfoils and their mechanism through numerical simulation.

In this study, the unsteady Reynolds-averaged Navier-Stokes- [17] (URANS-) based  $\gamma - \widetilde{Re}_{\theta t}$  transition model [17, 18] was used, and the time-averaged and unsteady aerodynamic characteristics of rounded trailing edge airfoils were numerically analyzed. First, the time-averaged characters of the DBLN-526 were calculated and compared with experiments. The results showed good agreement, indicating the reliability of the numerical simulation. Second, three different airfoils were compared with the DBLN-526. The unsteady characteristics of rounded trailing-edge airfoils were discussed in detail. Numerical results indicated that the unsteady force of the DBLN-526 airfoil was significantly smaller than that of the cambered-elliptic airfoil. Finally, to identify the cause of the lower lift fluctuation of DBLN-526, a mechanistic study was conducted. Mechanistic studies indicated that the two steps on the DBLN-526 airfoil lower surface were the reason for the lower lift fluctuation. Through these steps, the transition location of the DBLN-526 lower surface was fixed at  $x/c = 0.75$ , in a wide range of angles, and two stable vortices were obtained near the trailing edge. Unsteady air loads could be dramatically decreased by imposing a boundary layer transition to change the trailing edge separation from laminar to turbulent separation.

## 2. Wind Tunnel Test

The DBLN-526 airfoil (Figure 1) is one of the few publicly available modern rounded trailing-edge airfoils and is similar to the profile used on the X2TD, which has a maximum thickness of  $t/c = 26\%$ , 4% camber, and unique subtle “steps” on the lower surface between  $x/c = 0.25$  and  $x/c = 0.75$  [12].

Wind tunnel tests were performed on the NF-3 wind tunnel (Figure 2) of Northwestern Polytechnical University, Xi’an, China, which is a low-speed blow-down wind tunnel, at  $Re = 0.8 \times 10^6$ ,  $Re = 1.2 \times 10^6$ ,  $Re = 1.4 \times 10^6$ , and speed ranging from 20 m/s to 130 m/s.

The nominal inflow turbulence intensity was approximately 0.045%. The root mean square and the power spec-

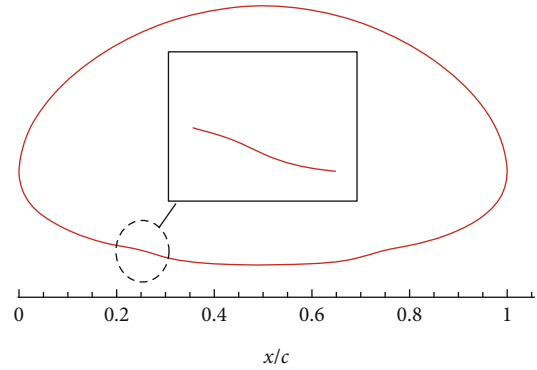


FIGURE 1: Profile of DBLN-526 airfoil.



FIGURE 2: DBLN-526 model in wind tunnel.

trum of the surface fluctuating pressure were used to judge the boundary layer transition in this experiment. Fifteen dynamic pressure sensors were installed on the upper and lower surface of the test model. Two kinds of pulsating pressure data were collected in the experiment: collected in the wind tunnel without wind as the zero-state pulsating pressure data of the sensor; after wind, the surface pulsating pressure of the model was collected as the original data for the analysis transition. The airfoil used in the test was a combination model of steel frame, wood structure, and aluminum alloy. The span length of the model was 1.593 m, and the chord length was 0.5 m. To reduce the sidewall interference, a spreading three-stage model was adopted, and the two outer segments of the model only supported and simulated the flow. The overall structure of the model is shown in Figure 3.

Under experimental conditions, the boundary layer remained laminar over a long range at both the upper and lower surfaces, and a trailing edge separation was constantly observable owing to the rounded trailing edge. The experimental results include the polar curve, pressure distribution, and transition position of the suction side. Due to relatively few dynamic pressure measuring points and interference of other signals, this test technique and data processing method need to be further improved. The experimental error of the transition onset position was approximately 0.1c.

## 3. Numerical Methods

All numerical simulations were performed with  $\gamma - \widetilde{Re}_{\theta t}$  transition model integrated into NASA Langley’s CFL3D

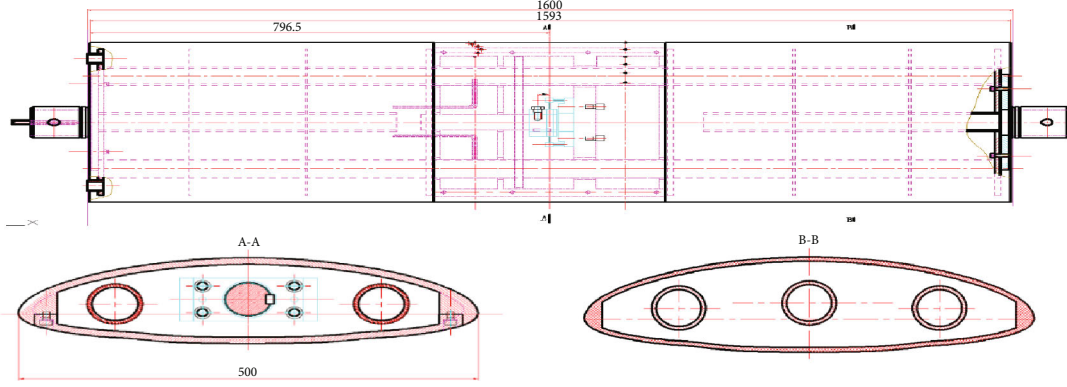


FIGURE 3: Model Structure.

[19] code, which is a three-dimensional structural grid solver based on a finite volume formulation. Time advance was performed by the dual-time stepping method; nonviscous fluxes were computed by MUSCL reconstruction and Roe's flux difference splitting scheme; viscous fluxes were calculated by second-order central differences. The freestream conditions are listed in Table 1. For time advance, where the dimensionless time step  $\Delta t/T$  was 0.025, the number of iterations was 6000, and that of subiterations was 30. The ambient source term method [20] was adopted to prevent inflow turbulence intensity from decaying before the leading edge. The governing equations are 3D unsteady RANS.

**3.1.  $\gamma - Re_{\theta t}$  Transition Model.** The  $\gamma - Re_{\theta t}$  transition model was proposed by Langtry and Menter and has achieved considerable success in different areas [18]. Different transition modes can be explained using different empirical correlations in this model, and all quantities need to be localized. Thus, this model is also called local correlation-based transition model. The parameters of the model used in this paper had been calibrated, and good results had been obtained in different transition problems [21].

Once the momentum thickness Reynolds number  $Re_{\theta}$  exceeds the transition onset momentum thickness Reynolds number  $Re_{\theta t}$ , the flow transitions from laminar to turbulent flow. The  $\gamma - Re_{\theta t}$  model can describe this process through two transport equations: the intermittency factor  $\gamma$  and the local transition onset momentum thickness Reynolds number  $\widetilde{Re}_{\theta t}$ , as follows:

$$\begin{aligned} \frac{\partial(\rho\gamma)}{\partial t} + \frac{\partial(\rho\gamma\bar{u}_j)}{\partial x_j} &= P_\gamma - E_\gamma + \frac{\partial}{\partial x_j} \left[ \left( \mu + \frac{\mu_t}{\sigma_\gamma} \right) \frac{\partial \gamma}{\partial x_j} \right], \\ \frac{\partial(\rho\widetilde{Re}_{\theta t})}{\partial t} + \frac{\partial(\rho\bar{u}_j\widetilde{Re}_{\theta t})}{\partial x_j} &= P_{\theta t} + \frac{\partial}{\partial x_j} \left[ \sigma_{\theta t}(\mu + \mu_t) \frac{\partial \widetilde{Re}_{\theta t}}{\partial x_j} \right]. \end{aligned} \quad (1)$$

The transition is triggered by  $\gamma$ , and empirical correlations can be localized through the transport equation for  $\widetilde{Re}_{\theta t}$ .  $P$  and  $E$  are the production and destruction terms for  $\gamma$  and  $\widetilde{Re}_{\theta t}$ , respectively. To improve the prediction ability

TABLE 1: Freestream conditions.

Ma	Re/10 <sup>6</sup>	$\alpha/(\circ)$	Tu%
0.1	0.8 1.2 1.4	-14-30	0.05

of the separation-induced transition of the model,  $\gamma$  had been modified and coupled with transport equation on turbulent kinetic energy of  $k - \omega$  SST turbulence model as follows:

$$\begin{aligned} \gamma_{\text{sep}} &= \min \left( s_1 \max \left[ 0, \left( \frac{Re_v}{3.325 Re_{\theta c}} \right) - 1 \right] F_{\text{reattach}}, 2 \right) F_{\theta t}, \\ \gamma_{\text{eff}} &= \max \left( \gamma, \gamma_{\text{sep}} \right), \\ \frac{\partial}{\partial t}(\rho k) + \frac{\partial}{\partial x_j}(\rho\bar{u}_j k) &= \widetilde{P}_k - \widetilde{D}_k + \frac{\partial}{\partial x_j} \left( (\mu + \sigma_k \mu_t) \frac{\partial k}{\partial x_j} \right), \\ \widetilde{P}_k &= \gamma_{\text{eff}} P_k; \quad \widetilde{D}_k = \min \left( \max \left( \gamma_{\text{eff}}, 0.1 \right), 1.0 \right) D_k, \end{aligned} \quad (2)$$

where  $P_k$  and  $D_k$  are original production and destruction term on turbulent kinetic energy of SST.  $\gamma_{\text{eff}}$  can judge the type of transition.

**3.2. Computational Grid.** The O-type structured grid shown in Figure 4 was used in all calculations in this study. To obtain independent solutions, three different levels of grids were generated, as listed in Table 2. All grids had  $y_{\text{max}}^+$  values less than 1. The transition locations all moved backward regardless of the upper or lower surface as the magnitude of the grid increased. Different pressure distributions of the three grids were compared with the experiments and are shown in Figure 5. The comparison indicated that medium and fine grids had an almost unanimous distribution and were in good agreement with the experiment in the trend, particularly at 0.72c-0.76c on both upper and lower surfaces. The friction distributions of different grids are shown in Figure 6, the transition locations obtained by medium and fine grid differed very little. Considering the calculation cost and accuracy, all subsequent calculations were performed on a medium grid, where 281 points were distributed on both the upper and lower surfaces; the far field was 500 chord

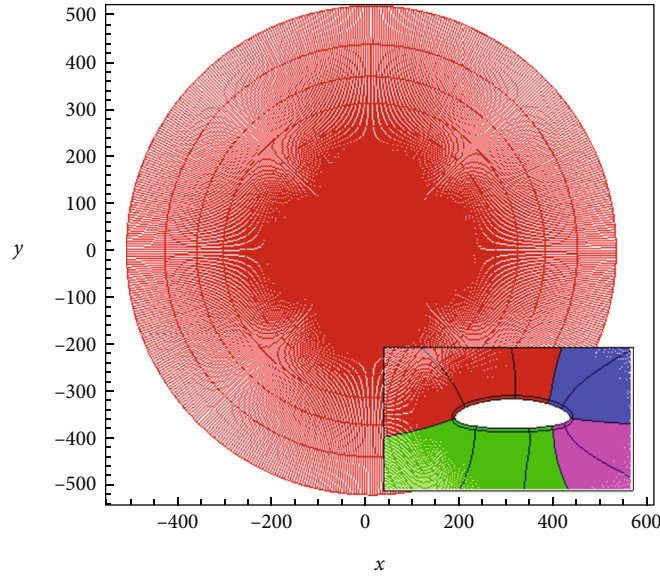


FIGURE 4: Structural grid.

TABLE 2: Grid information ( $Re = 1.4 \times 10^6$ ).

Level	Points on airfoil	Nodes	First spacing	$y^+_{max}$	Transition location (upper)	Transition location (lower)
Coarse	292	82844	$1 \times 10^{-5}$	0.832	0.716c	0.719c
Medium	588	165132	$5 \times 10^{-6}$	0.371	0.740c	0.730c
Fine	824	254160	$2.5 \times 10^{-6}$	0.208	0.743c	0.733c
Exp	\	\	\	\	\	0.750c

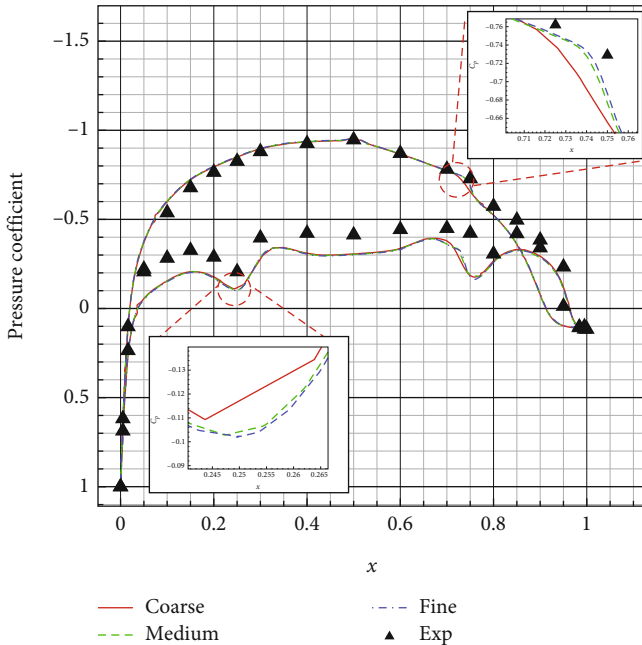


FIGURE 5: Pressure distribution ( $Re = 1.4E6, \alpha = 2^\circ$ ).

lengths; the first grid height was  $5 \times 10^{-6}$  ensuring  $y^+ < 1$  at the wall. The grid contained 165132 points in total and was encrypted at the leading and trailing edges of the airfoil as well as at the flats, as shown in Figures 4 and 7.

#### 4. Results and Discussion

4.1. Time Averaged Aerodynamic Characteristics. The streamlines in Figure 8 indicate that the two eddies were fixed behind the trailing edge of the DBLN-526 airfoil because of its profile. In addition, there was a separation bubble on the lower surface from 0.70c to 0.75c, which caused by the adverse pressure gradient. As shown in Figure 9, the separation bubble caused a flow transition. Plots of the angle of attack versus lift and drag coefficients are shown in Figures 10 and 11 respectively. For lift coefficients, the experiment showed two linear regions between  $-14^\circ$  and  $8^\circ$ , which were captured well by numerical solutions. From  $-14^\circ$  to  $0^\circ$ , the numerical solutions were slightly lower than those of the experiment, and for the second linear region from  $0^\circ$  to  $8^\circ$ , the computational fluid dynamics (CFD) solutions were almost the same as those in the experiment. The lift coefficient at stall evaluated by CFD was larger than that in the experiment. As for the drag coefficients, the CFD solutions and experiments were in very good agreement except between  $24^\circ$  and  $30^\circ$ , where massive flow

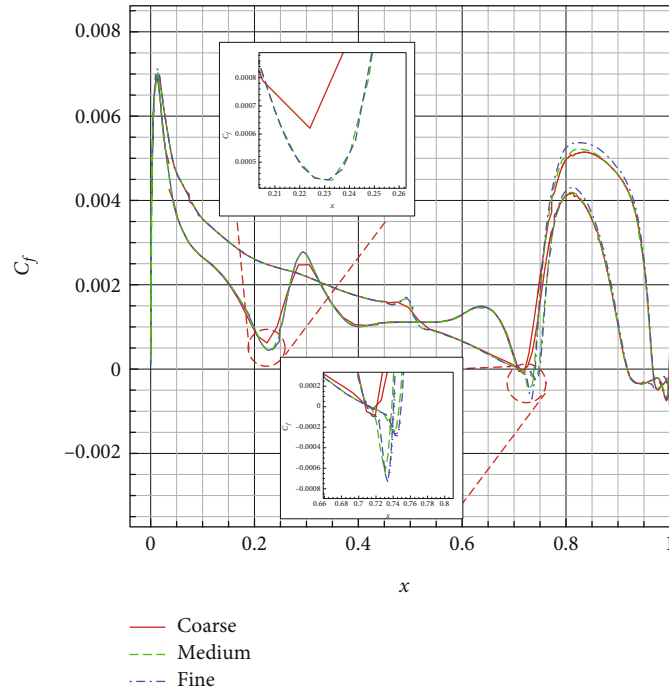


FIGURE 6: Friction distribution ( $Re = 1.4E6, \alpha = 2^\circ$ ).

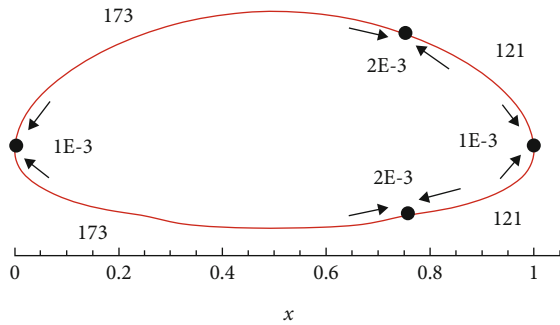


FIGURE 7: Grid distribution for medium grid.

separation occurred, and the URANS method was not efficient, but the transition DDES method can provide good solutions [15]. Here, we do not discuss the characteristics of DBLN-526 at a high angle of attack; thus, the URANS is sufficient for simulation. Comparisons between the numerical and experimental results proved the reliability of the numerical methods adopted in this study.

**4.2. Unsteady Aerodynamic Character of Rounded Trailing Edge Airfoils.** The unsteady characteristics of airfoils are very important for the design of a coaxial rotor. Because of the separation at the rounded trailing edge, the flow around a rounded trailing edge airfoil is unsteady by nature, and the air loads are unsteady. Unsteady air loads may lead to vibration and noise and increase the fatigue of the blades, hub, and pitch links [8]. The unsteady aerodynamic character quantified by  $\Delta C_l$ , which is defined as the maximum lift coefficient minus the minimum lift coefficient when the

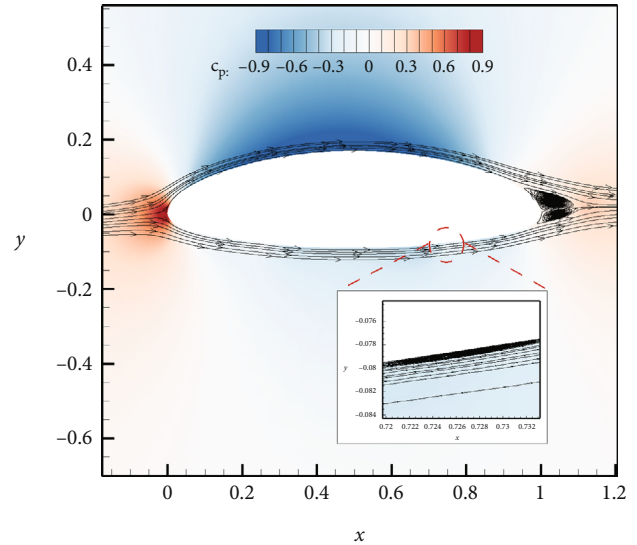


FIGURE 8: Pressure contour and streamlines ( $Re = 1.4E6, \alpha = 2^\circ$ ).

oscillation amplitude is constant. In the following calculations,  $\Delta C_l$  was calculated using the last 1000 steps.

The unsteady aerodynamic characteristics of two typical rounded trailing edge airfoils were compared: DBLN-526 airfoil and elliptic airfoil with  $t/c = 26\%$  and 4% camber (herein after denoted as Elliptic264). The geometries of these two airfoils are compared in Figure 12. The overall geometries of these two airfoils are very similar, with only minor differences on the upper side. Their primary differences are located at the lower side, where a “step” exists between  $x/c = 0.25$  and  $x/c = 0.75$  in DBLN-526 airfoil, whereas

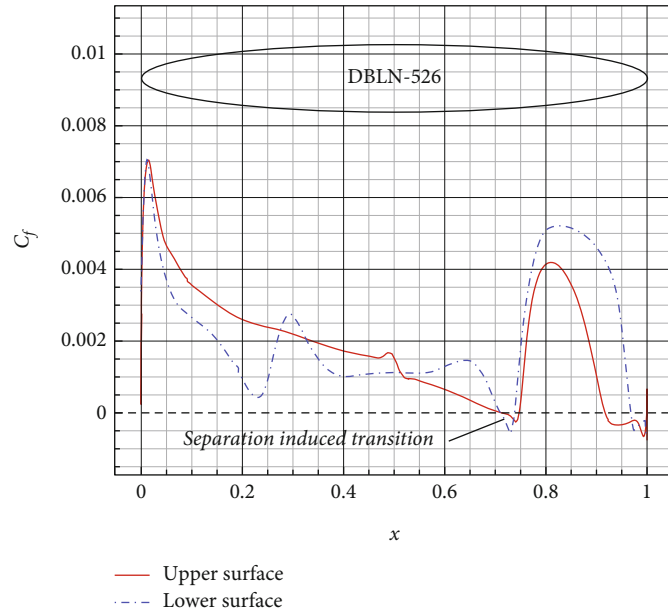


FIGURE 9: Skin friction distribution ( $Re = 1.4E6$ ,  $\alpha = 2^\circ$ ).

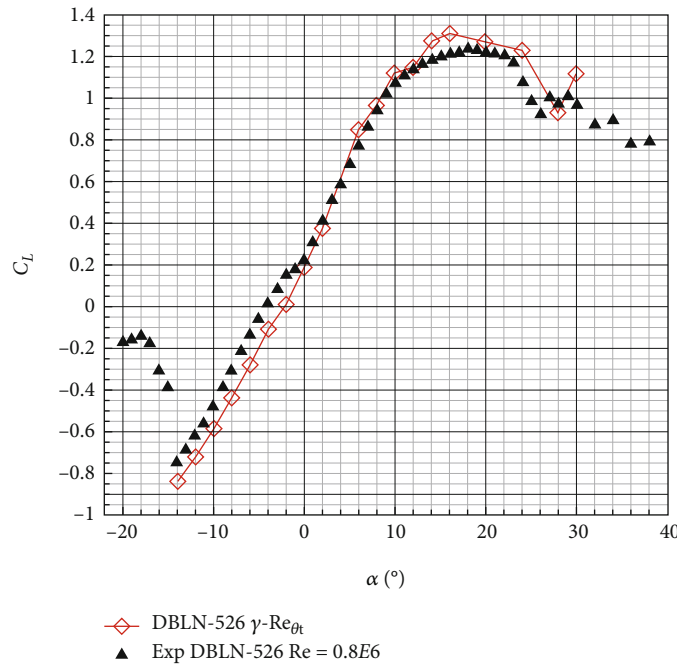


FIGURE 10: Lift coefficient of DBLN-526 airfoil ( $Re = 0.8E6$ ).

Elliptic264 is smooth. The time-averaged pressure distributions of the DBLN-526 and Elliptic264 airfoils at  $Re = 0.8 \times 10^6$  and  $Re = 1.4 \times 10^6$ , and  $\alpha = 2^\circ$  and  $\alpha = 6^\circ$  are shown in Figures 13 and 14, respectively. The numerical results for DBLN-526 were in good agreement with the experimental results; thus, although differences were observed due to trailing edge separation, the numerical results represented the primary characteristics of DBLN-526 airfoils. The transition locations for DBLN-526 and Elliptic264 at different  $Re$  values were compared with the experiments trends in

Figures 15 and 16. For the same  $Re$  values, the transition locations at the lower surfaces of the two airfoils moved backward with an increase in the angle of attack. All the computational transition locations were within the margin of experimental error ( $0.1c$ ). For  $Re = 0.8 \times 10^6$ , from  $-14^\circ$  to  $-2^\circ$ , the two foils had almost the same transition locations, and after  $-2^\circ$ , the transition location of DBLN-526 was fixed at  $0.75c$  until  $4^\circ$ , where the transition location started moving backward again. For Elliptic264, the transition location moved backward to  $0^\circ$ . The transition location “step” for

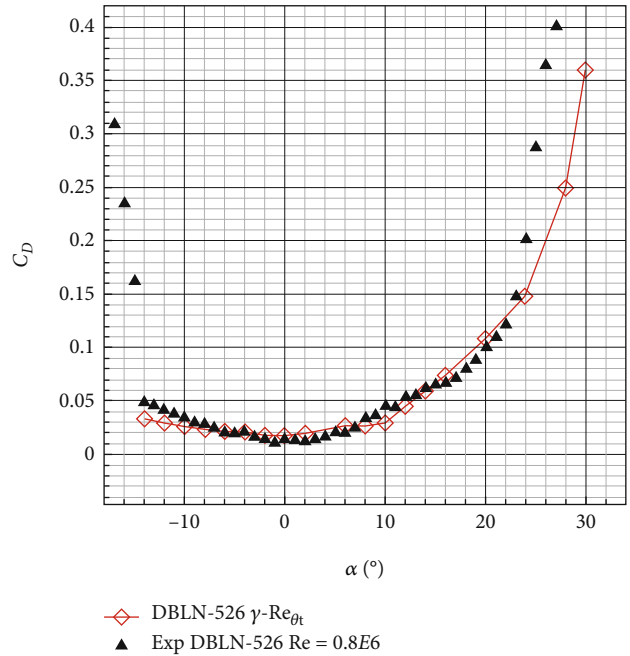


FIGURE 11: Drag coefficient of DBLN-526 airfoil ( $Re = 0.8E6$ ).

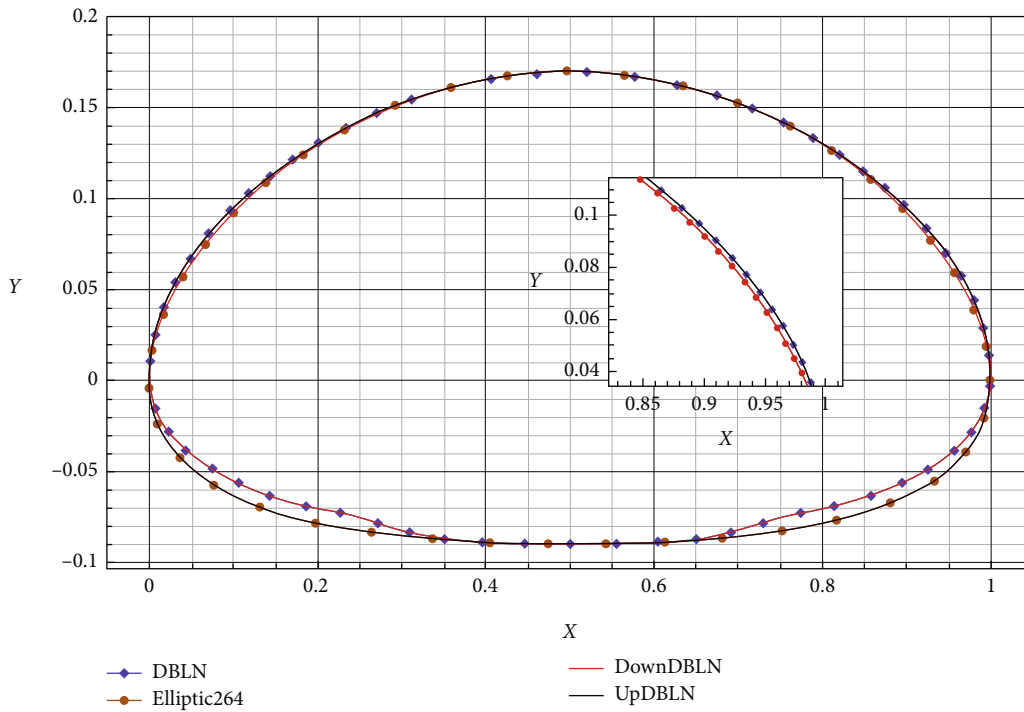


FIGURE 12: Profiles of airfoil section used in the present study.

DBLN-526 was captured well by CFD. For  $Re = 1.4 \times 10^6$ , the transition locations for Elliptic264 were behind those of DBLN-526, and the difference was large. The “step” of DBLN-526 started from  $0^\circ$  to  $10^\circ$ , whereas the experiment showed that the “step” started from  $3^\circ$  to  $8^\circ$ . Transition locations after the “step” captured by experiment for DBLN-526 were behind those of the CFD solutions. The computational results were all within the margin of error.

The  $\Delta Cl$  at  $Re = 0.8 \times 10^6$ ,  $Re = 1.2 \times 10^6$ ,  $Re = 1.4 \times 10^6$  were computed and results are listed in Tables 3 and 4 and compared in Figure 17. Although only minor differences were observed in the geometries, differences in unsteady characteristics were significant. The  $\Delta Cl$  of Elliptic264 was one or two orders of magnitude higher than that of the DBLN-526 airfoil. The DBLN-526 airfoil was evidently better than elliptic airfoils in terms of unsteady characteristics.

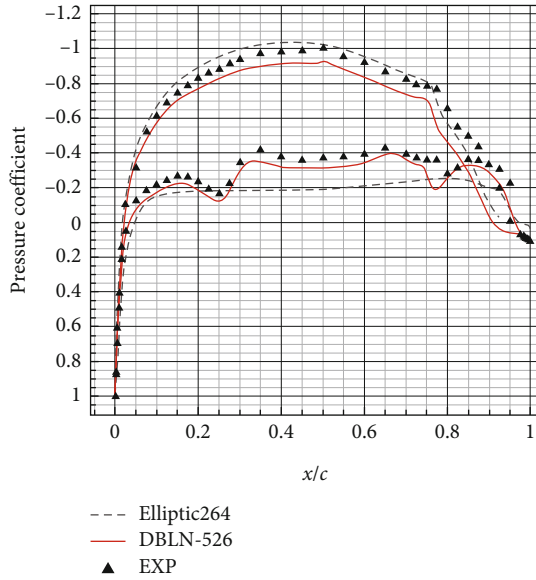


FIGURE 13: Pressure distribution ( $Re = 0.8E6, \alpha = 2^\circ$ ).

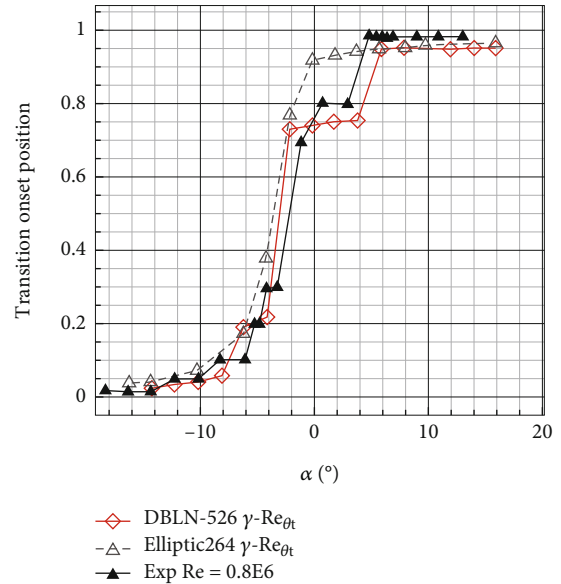


FIGURE 15: Lower surface transition position ( $Re = 0.8E6$ ).

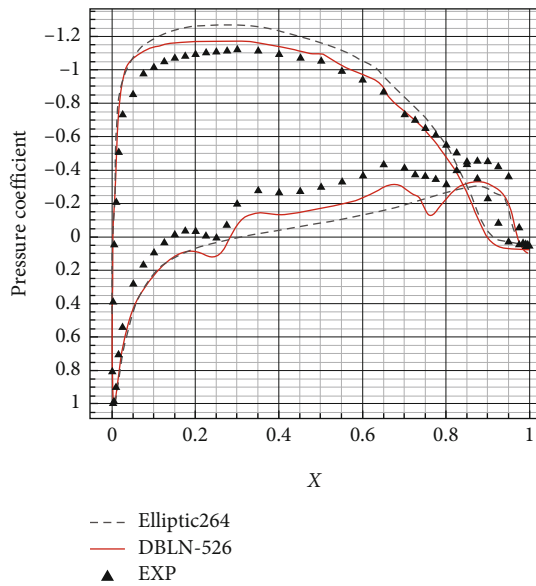


FIGURE 14: Pressure distribution ( $Re = 1.4E6, \alpha = 6^\circ$ ).

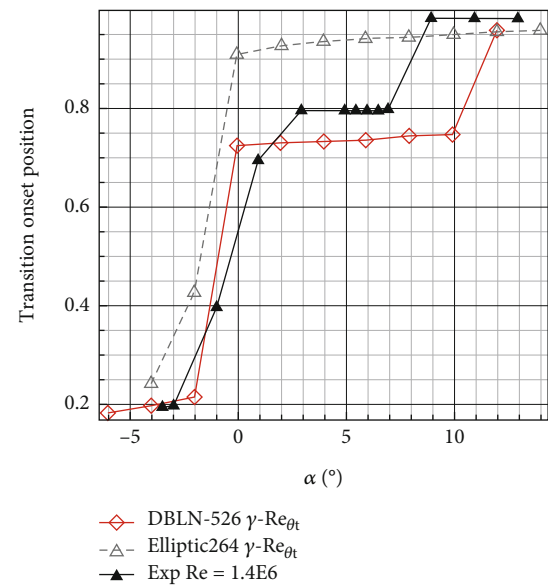


FIGURE 16: Lower surface transition position ( $Re = 1.4E6$ ).

Figure 18 shows a comparison of the power spectral density (PSD) of the two airfoils at  $Re = 0.8 \times 10^6, \alpha = 0^\circ$ , where the Strouhal number was calculated by  $St = fL_0/U_0$ ,  $L_0$  adopts 1 m, and  $U_0$  adopts  $Ma$  times the speed of sound (334.22 m/s). The peak values for Elliptic264 and DBLN-526 were  $St = 2.33PSD = 1.72E - 1$ , and  $St = 2.54PSD = 1.98E - 5$ , respectively. The peak value of Elliptic264 was four orders of magnitude higher than that of DBLN-526, indicating a considerably stronger oscillation of Elliptic264 than DBLN-526 in lift coefficients. The PSD analysis was consistent with  $\Delta Cl$  calculations.

4.3. Further Investigation on Unsteady Characters of Rounded Trailing Edge Airfoils. Flow separation near the trailing edge is the characteristic of rounded trailing edge

airfoils. Boundary layer separation leads to a decrease in lift and an increase in drag. In addition, flow separation results in oscillation, buffet, noise, etc. This problem is particularly common at low Reynolds' numbers when laminar flow is prevalent [22] For practical rounded trailing edge airfoils, it is crucial to alleviate unsteady air loads by reducing flow separation, and the superiority of the DBLN-526 airfoil in terms of unsteady characteristics is prominent from the results above.

To locate the source of the differences in  $\Delta Cl$ , the influences of the upper and lower surfaces were studied individually. Two other test airfoils were constructed: UpDBLN and DownDBLN (Figure 12). UpDBLN was composed of the upper surface of the DBLN-526 airfoil and the lower surface of the Elliptic264 airfoil; DownDBLN was composed of the

TABLE 3:  $\Delta Cl$  for DBLN-526 airfoil.

Reynolds number	-6°	-4°	-2°	0°	2°	4°	6°	8°	10°
$Re = 0.8 \times 10^6$	$2.2E-4$	$4.2E-4$	$7.6E-4$	$9.5E-4$	0.0012	0.0013	0.0024	0.0027	0.0038
$Re = 1.2 \times 10^6$	$4.5E-4$	$8.2E-4$	$6.8E-4$	$8.2E-4$	$9.5E-4$	$4.0E-4$	$8.6E-4$	0.0013	0.0010
$Re = 1.4 \times 10^6$	$2.6E-4$	$4.9E-4$	$5.6E-4$	$8.9E-4$	$4.2E-4$	$7.1E-4$	$4.5E-4$	$3.9E-4$	0.0010

TABLE 4:  $\Delta Cl$  for Elliptic264 airfoil.

Reynolds' number	-6°	-4°	-2°	0°	2°	4°	6°	8°	10°
$Re = 0.8 \times 10^6$	0.0027	0.0023	0.0246	0.0407	0.0566	0.0629	0.0610	0.0482	0.0293
$Re = 1.2 \times 10^6$	0.0022	0.0075	0.0074	0.0276	0.0490	0.0549	0.0485	0.0355	0.0256
$Re = 1.4 \times 10^6$	0.0043	0.0117	0.0099	0.0357	0.0432	0.0446	0.0432	0.0329	0.0163

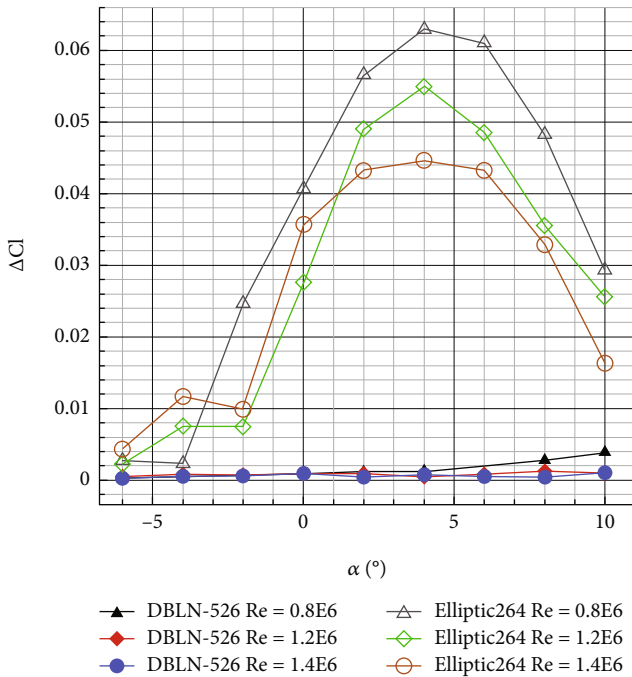


FIGURE 17: Comparison of  $\Delta Cl$  for two airfoils.

upper surface of the Elliptic264 airfoil and the lower surface of the DBLN-526 airfoil. The inflow conditions were the same as those described in Section 4.2. The calculated  $\Delta Cl$  values of the four airfoils are listed in Tables 5–7 and are compared in Figure 19. The time histories of the lift coefficients are compared in Figure 20.

As can be seen in Figure 19, when  $-6^\circ < \alpha < 4^\circ$ , the  $\Delta Cl$  values of DBLN-526 and DownDBLN were very similar as well as those of Elliptic264 and UpDBLN. When  $\alpha > 4^\circ$ , the  $\Delta Cl$  of DownDBLN increased dramatically to the magnitudes of Elliptic264 and UpDBLN. From all the tables, the  $\Delta Cl$  of DownDBLN had a rapid change around  $\alpha = 0^\circ$ . For Elliptic264 and UpDBLN, the  $\Delta Cl$  increased dramatically after  $\alpha = -4^\circ$  and reached a peak value near  $\alpha = 4^\circ - 6^\circ$ .

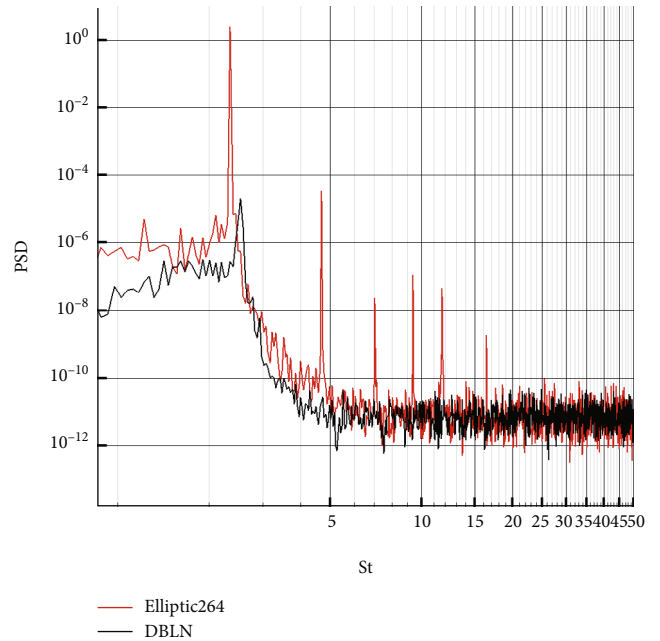


FIGURE 18: PSD of lift coefficient ( $Re = 0.8E6, \alpha = 0^\circ$ ).

The time history of the lift coefficient of the four airfoils indicates that the lift coefficient changes of the DBLN-526 and DownDBLN airfoils were of the same order and were considerably smaller than those of the Elliptic264 and UpDBLN airfoils. The lift coefficient time history was consistent with  $\Delta Cl$  calculations and confirmed the reliability of  $\Delta Cl$  calculations. When  $Re = 0.8 \times 10^6$ , comparisons between the four airfoils indicated that  $-6^\circ < \alpha < 6^\circ$ ; the low  $\Delta Cl$  was a result of the lower surface of the DBLN-526 airfoil, whereas at  $\alpha \geq 6^\circ$ ; it was more connected to the upper surface of the DBLN-526 airfoil. This conclusion was further supported by the power spectral analyses plotted in Figures 21 and 22. These analyses showed similarities between UpDBLN and Elliptic264 and between DownDBLN and DBLN-526.

TABLE 5: Comparisons of  $\Delta Cl$  at  $Re = 0.8 \times 10^6$ .

Airfoil	-6°	-4°	-2°	0°	2°	4°	6°	8°	10°
DBLN-526	$2.2E-4$	$4.2E-4$	$7.6E-4$	$9.5E-4$	0.0012	0.0013	0.0024	0.0027	0.0038
Elliptic264	0.0027	0.0023	0.0246	0.0407	0.0566	0.0629	0.0610	0.0482	0.0293
DownDBLN	$4.0E-4$	$5.3E-4$	0.0013	0.0036	$9.2E-4$	0.0011	0.0483	0.0309	0.0279
UpDBLN	0.0077	0.0011	0.0047	0.0406	0.0509	0.0626	0.0655	0.0450	0.0374

TABLE 6: Comparisons of  $\Delta Cl$  at  $Re = 1.2 \times 10^6$ .

Airfoil	-6°	-4°	-2°	0°	2°	4°	6°	8°	10°
DBLN-526	$4.5E-4$	$8.2E-4$	$6.8E-4$	$8.2E-4$	$9.5E-4$	$4.0E-4$	$8.6E-4$	0.0013	0.0010
Elliptic264	0.0022	0.0075	0.0074	0.0276	0.0490	0.0549	0.0485	0.0355	0.0256
DownDBLN	$5.8E-4$	$4.5E-4$	0.0015	0.0095	0.0013	$8.0E-4$	0.0015	0.0012	0.0056
UpDBLN	0.0013	$8.6E-4$	0.0028	0.0239	0.0485	0.0518	0.0490	0.0365	0.0347

TABLE 7: Comparisons of  $\Delta Cl$  at  $Re = 1.4 \times 10^6$ .

Airfoil	-6°	-4°	-2°	0°	2°	4°	6°	8°	10°
DBLN-526	$2.6E-4$	$4.9E-4$	$5.6E-4$	$8.9E-4$	$4.2E-4$	$7.1E-4$	$4.5E-4$	$3.9E-4$	0.0010
Elliptic264	0.0043	0.0117	0.0099	0.0357	0.0432	0.0446	0.0432	0.0329	0.0163
DownDBLN	$2.6E-4$	$3.2E-4$	$3.9E-4$	0.0014	0.0012	$6.3E-4$	0.0012	0.0012	0.1065
UpDBLN	$2.9E-4$	$8.3E-4$	0.0014	0.0217	0.0440	0.0506	0.0446	0.0349	0.0229

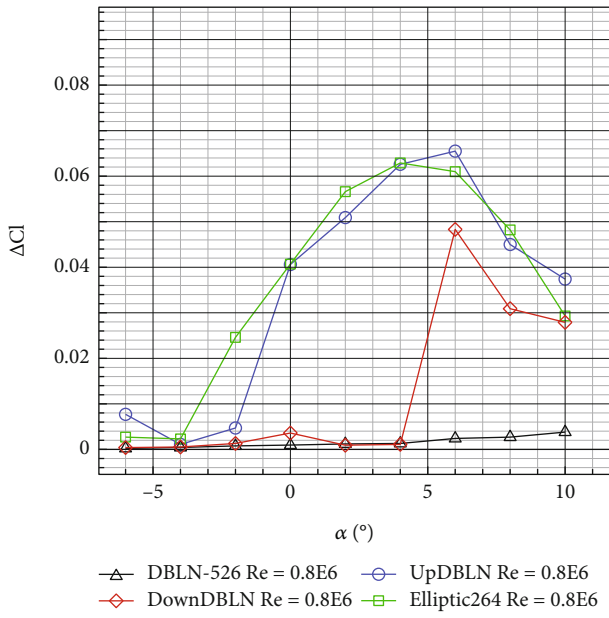


FIGURE 19: Comparisons of  $\Delta Cl(Re = 0.8E6)$ .

The transition onset positions of the four airfoils are compared in Figures 23 and 24 ( $Re = 0.8 \times 10^6$ ). At the upper surface, the transition onset positions moved forward with the increase of the angle of attack, and the four airfoils had very similar transition onset positions. DBLN-526 and UpDBLN had almost the same transition onset positions at the upper surface, whereas those of DownDBLN were

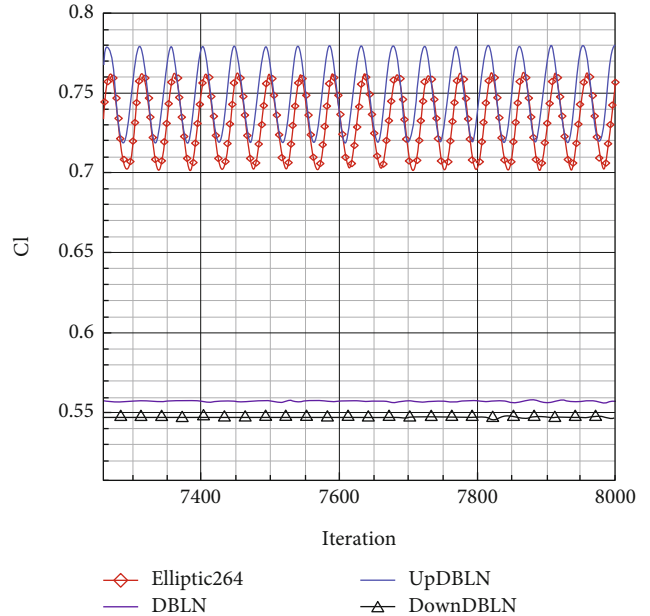


FIGURE 20: Lift coefficients ( $Re = 0.8E6, \alpha = 4^\circ$ ).

behind those of Elliptic264. This indicates that the upper surface of DBLN-526 was a key point for low  $\Delta Cl$  after  $\alpha = 6^\circ$ . At the lower surface, the transition positions for Elliptic264 and UpDBLN were very similar and varied smoothly with the angle of attack. DBLN-526 and DownDBLN airfoils had similar transition onset positions at  $\alpha = 6^\circ$ ; at  $\alpha = 4^\circ$ , transition occurred at approximately  $x/c = 0.25$ ; it increased

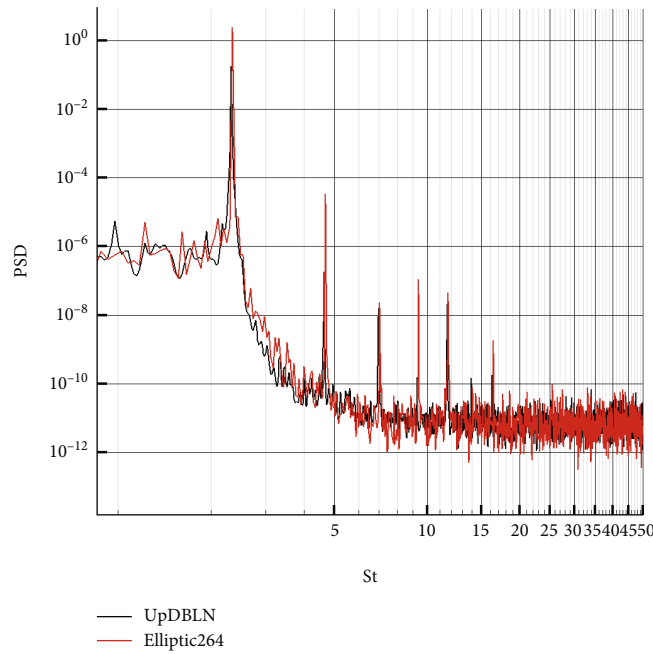


FIGURE 21: PSD of UpDBLN and Elliptic264 ( $Re = 0.8E6, \alpha = 0^\circ$ ).

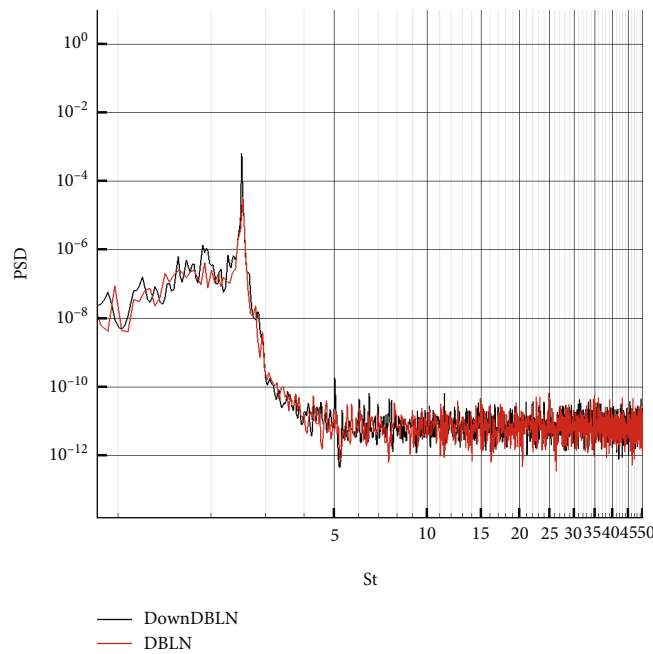


FIGURE 22: PSD of DownDBLN and DBLN-526 ( $Re = 0.8E6, \alpha = 0^\circ$ ).

suddenly from  $x/c = 0.2$  to approximately  $x/c = 0.75$  at  $\alpha = -2^\circ$ ; it remained at  $x/c = 0.75$  until  $\alpha = 6^\circ$  for DownDBLN and  $\alpha = 8^\circ$  for DBLN-526. Subsequently, the transition position jumped to approximately  $x/c = 0.95$ . The transition positions for DBLN-526 and DownDBLN had two relative fixed positions ( $x/c = 0.25$  and  $x/c = 0.75$ ), which were in accordance with the “step” position of the lower surface of the DBLN-526 airfoil. The unique transition phenomenon was attributed to the adverse pressure gradient caused by the “step.”

As can be seen in Figure 25, the pressure coefficient distribution showed that the “step” caused strong adverse pressure gradient at approximately  $x/c = 0.25$  and  $x/c = 0.75$ . This was also indicated by the distribution of the pressure gradient parameter  $\lambda_\theta$  shown in Figure 26. The definition of  $\lambda_\theta$  is given in Equation (3) and is calculated using the  $\gamma - Re_{\theta t}$  transition model. Where the  $\rho$  is density,  $\theta$  is momentum thickness of boundary layer,  $\mu$  is molecular viscosity,  $U$  is local velocity, and  $s$  is direction of streamlines.

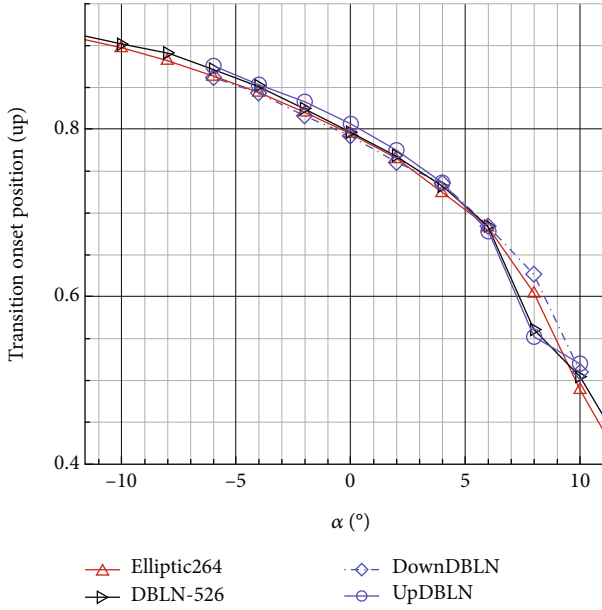


FIGURE 23: Transition onset position (upper surface).

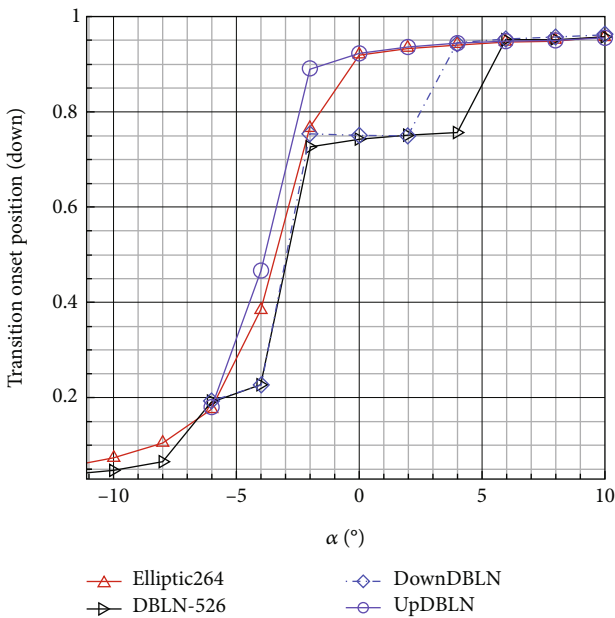


FIGURE 24: Transition onset position (lower surface).

$$\lambda_\theta = \frac{\rho\theta^2}{\mu} \frac{dU}{ds}. \quad (3)$$

In Figure 26, the pressure drop region is indicated by  $\lambda_\theta > 0$ , and the pressure increase region is indicated by  $\lambda_\theta < 0$ . Two strong adverse pressure gradient regions are observed, located at  $0.15 < x/c < 0.25$  and  $0.68 < x/c < 0.75$ .

Therefore, it can be concluded that the “step” at the lower surface had a significant influence on the transition position, and the transition position had a significant influence on the unsteady aerodynamic characteristics. The influence of the

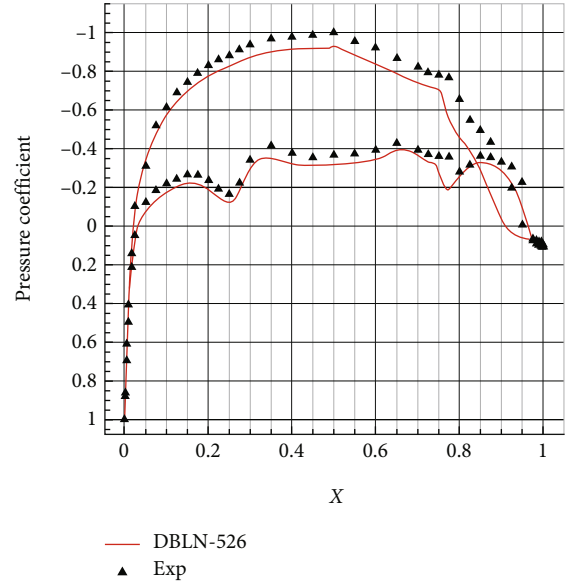


FIGURE 25: Pressure distribution ( $Re = 0.8E6$ ,  $\alpha = 2^\circ$ ).

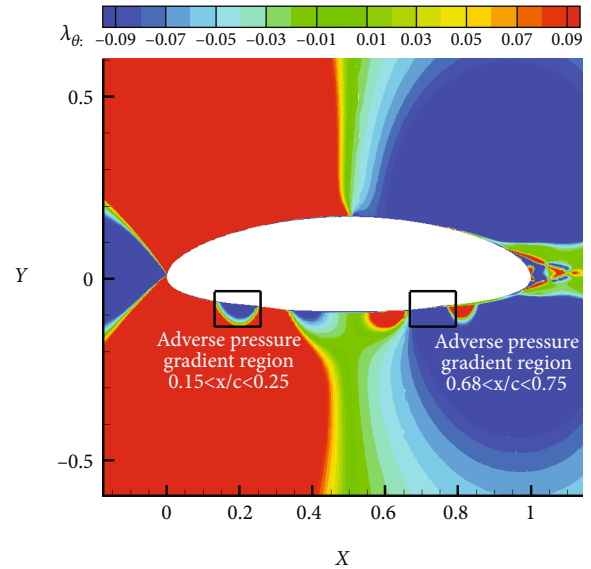


FIGURE 26:  $\lambda_\theta$  distribution for DBLN ( $Re = 0.8E6$ ,  $\alpha = 0^\circ$ ).

transition on unsteady aerodynamic characteristics was investigated as follows. Figures 27–30 show the skin friction, turbulence kinetic distributions, and streamlines of the DBLN-526 and Elliptic264 airfoils at  $Re = 0.8 \times 10^6$  and  $\alpha = 0^\circ$ . For the lower surface of the DBLN-526 airfoil, the flow transition at  $x/c = 0.75$  through a separation bubble and the boundary layer became a turbulence boundary layer, which remained attached until turbulent separation near  $x/c = 0.97$ . Two stable separation vortices were observed at the trailing edge. For the Elliptic264 airfoil, laminar separation occurred at  $x/c = 0.85$ , and the transition occurred at  $x/c = 0.92$ . This laminar separation occurred earlier than the turbulent separation, which was still observed near the trailing

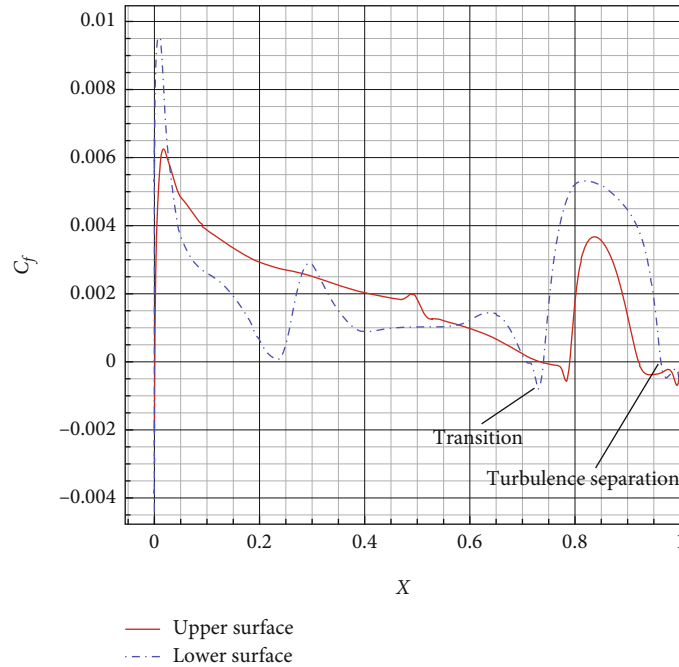


FIGURE 27: Skin friction distribution of DBLN-526 airfoil ( $Re = 0.8E6$ ,  $\alpha = 0^\circ$ ).

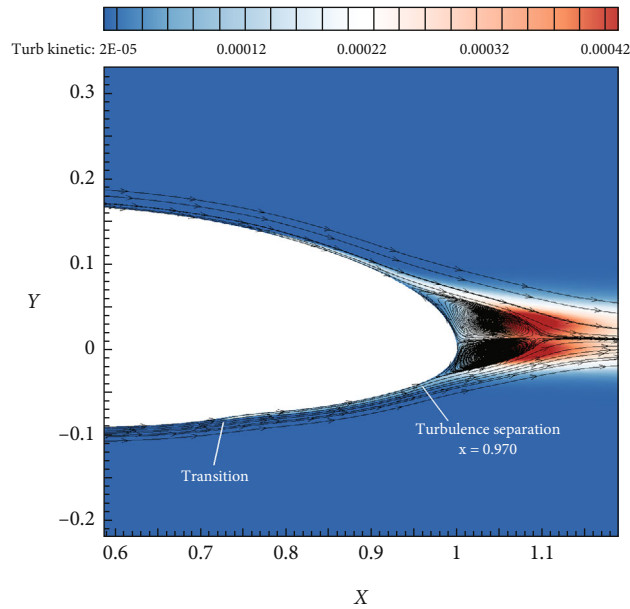


FIGURE 28: Turbulent kinetic energy distribution of DBLN-526 airfoil ( $Re = 0.8E6$ ,  $\alpha = 0^\circ$ ).

edge. The vortices at the trailing edge were unstable, and vortex shedding was observed during the calculation.

At  $Re = 0.8 \times 10^6$  and  $\alpha = 0^\circ$ , the time-averaged turbulence kinetics  $k_{ave}$  at  $d_{wall} = 1.75E - 4$ , which was approximately at the center of the boundary layer, is tabulated in Table 8 and compared in Figure 31. It can be seen that after the transition at  $x/c = 0.75$ , the turbulence kinetics of the DBLN-526 and DownDBLN airfoils significantly increased, which improved the ability of the boundary layer to resist

separation. The changes in the pressure and friction coefficients at the lower surface are listed in Table 9. The pressure and friction coefficients changes of the DBLN-526 and DownDBLN airfoils were one order of magnitude lower than those of the UpDBLN airfoil, which may be due to the relatively stable turbulence boundary. This tendency can also be observed in Figures 32 and 33, where the magnitude of UpDBLN was evidently higher than that of the DBLN-526 and DownDBLN airfoils.

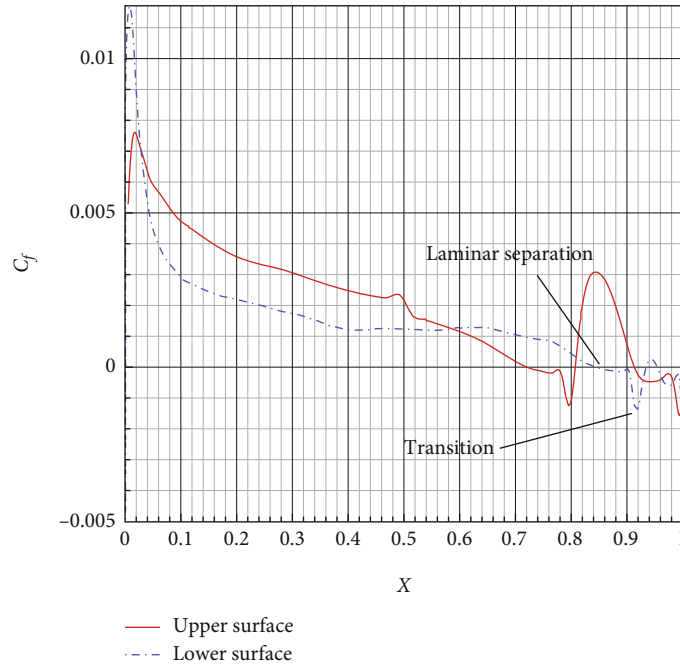


FIGURE 29: Skin friction distribution of Elliptic264 airfoil ( $Re = 0.8E6, \alpha = 0^\circ$ ).

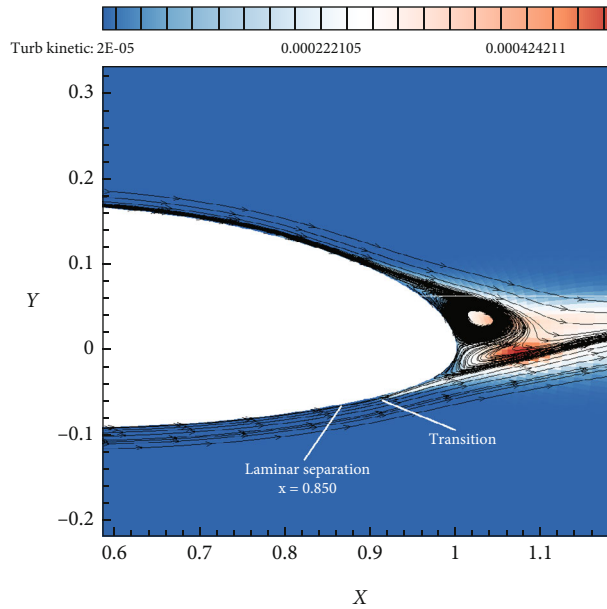


FIGURE 30: Turbulent kinetic energy distribution of Elliptic264 airfoil ( $Re = 0.8E6, \alpha = 0^\circ$ ).

The law of turbulent kinetic energy of boundary layer with transition is that turbulent kinetic energy in the laminar flow region is zero and rapidly increases to the peak at transition and gradually decreases with the downward development of the flow in the subsequent turbulent boundary layer. As shown in Figures 34 and 35, the transition location moved upstream with the increase of  $Re$ . According to the change law of turbulent kinetic energy in the boundary layer, the turbulent kinetic energy of earlier transition is less than that of later transition at the same station. This can be con-

firmed in turbulent kinetic energy clouds. Thus, the distance of transition position before separation significantly affects the size of separation zone. Slightly ahead of the transition position of separation injects a lot of energy into the boundary layer, weakening the separation. The change of the separation zone will obviously change the overall pressure distribution, lift, and drag law. The separation of the DBLN-526 airfoil was affected by the transition position, resulting in its aerodynamic characteristics that were sensitive to the turbulence and Reynolds' number of the incoming flow.

TABLE 8: Time-averaged turbulence kinetics  $k_{ave}$  ( $Re = 0.8 \times 10^6$  and  $\alpha = 0^\circ$ ).

$x/c$	0.60	0.65	0.75	0.80	0.85	0.90	0.95
DBLN-526	$3.89E-10$	$3.85E-10$	$1.65E-04$	$1.26E-04$	$9.23E-05$	$8.61E-05$	$8.38E-05$
DownDBLN	$3.68E-10$	$3.67E-10$	$1.66E-04$	$1.26E-04$	$9.30E-05$	$8.63E-05$	$8.43E-05$
UpDBLN	$4.15E-10$	$5.80E-10$	$1.63E-09$	$3.24E-09$	$1.46E-08$	$8.14E-07$	$1.05E-04$

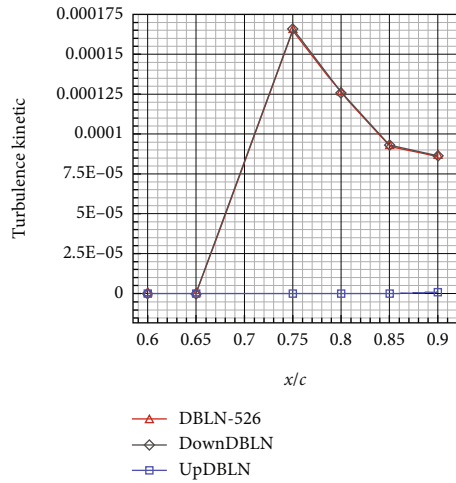


FIGURE 31: Turbulence kinetic ( $Re = 0.8E6$ ,  $\alpha = 0^\circ$ ).

TABLE 9: Changes of pressure and friction coefficients ( $Re = 0.8 \times 10^6$  and  $\alpha = 0^\circ$ ).

$x/c$	DBLN-526		DownDBLN		UpDBLN	
	$\Delta C_f$	$\Delta C_p$	$\Delta C_f$	$\Delta C_p$	$\Delta C_f$	$\Delta C_p$
0.60	$2.96E-07$	0.0007	$9.25E-07$	0.0030	$8.90E-06$	0.0251
0.65	$5.45E-07$	0.0008	$1.23E-06$	0.0033	$1.13E-05$	0.0267
0.70	$1.10E-06$	0.0008	$2.67E-06$	0.0036	$1.50E-05$	0.0290
0.75	$1.59E-05$	0.0013	$2.20E-05$	0.0038	$2.09E-05$	0.0319
0.80	$5.16E-06$	0.0010	$1.10E-05$	0.0043	$3.44E-05$	0.0368
0.85	$3.66E-06$	0.0012	$1.58E-05$	0.0052	$6.41E-05$	0.0444
0.90	$5.37E-06$	0.0015	$1.85E-05$	0.0068	$1.49E-04$	0.0586

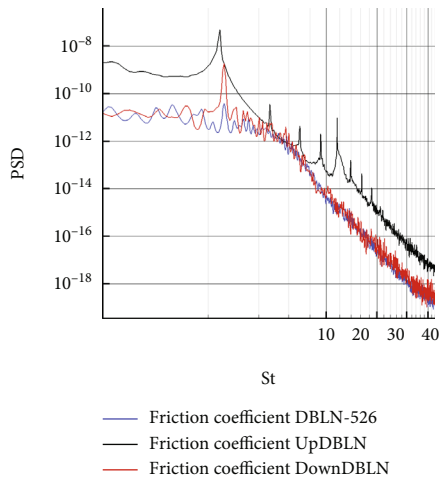


FIGURE 32: PSD of friction coefficient ( $Re = 0.8E6$ ,  $\alpha = 0^\circ$ ).

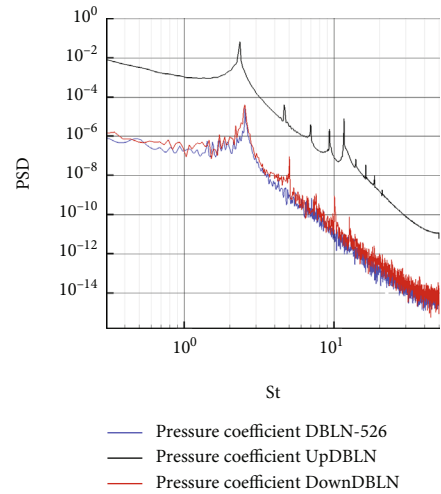


FIGURE 33: PSD of pressure coefficient ( $Re = 0.8E6$ ,  $\alpha = 0^\circ$ ).

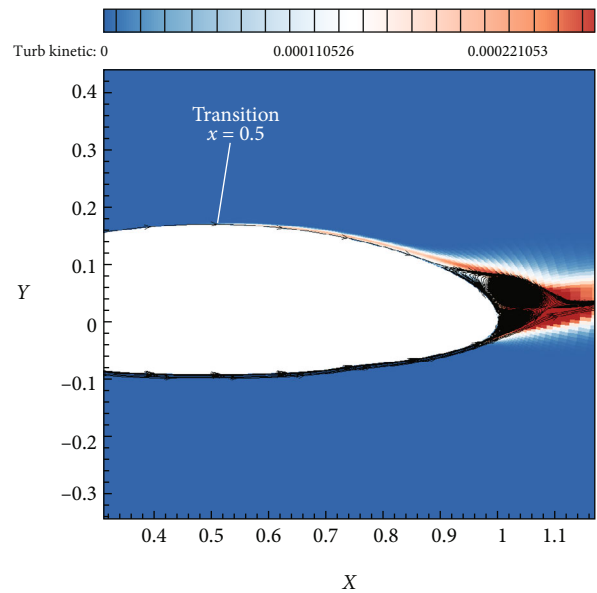


FIGURE 34: Turbulent kinetic energy distribution of DBLN-526 airfoil ( $Re = 0.8E6$ ,  $\alpha = 10^\circ$ ).

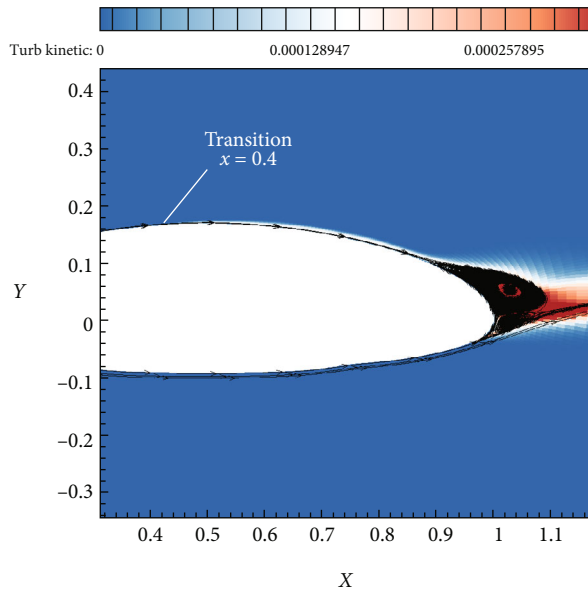


FIGURE 35: Turbulent kinetic energy distribution of DBLN-526 airfoil ( $Re = 1.4E6$ ,  $\alpha = 10^\circ$ ).

## 5. Conclusions

In this study, the unsteady characteristics of rounded trailing edge airfoils were analyzed, and the mechanism of the superior unsteady characteristics of DBLN-526 airfoil was revealed. Numerical simulations were conducted with the URANS-based  $\gamma - \widetilde{Re}_{\theta t}$  model. From the studies on the mechanism of the superior unsteady characters of DBLN-526 airfoil, three conclusions were drawn: (1) the superiority of DBLN-526 airfoil in terms of unsteady aerodynamic characters was caused by its unique lower surface design, that is, the “step”, which extends from  $x/c = 0.25$  to  $x/c = 0.75$ . (2) the primary function of this “step” is to control the transition onset positions. The adverse pressure gradient caused by this step at  $x/c = 0.75$  led to a flow transition at  $x/c = 0.75$  for a relatively large range of angles of attack. In addition, the early transition caused by the “step” changed the separation type at trailing edge from laminar to turbulent separation. The fixed transition positions can prevent interaction from the change of transition positions and separation. (3) turbulent separation was more stable and caused less unsteady air loads than laminar separation, and the turbulent separation region was smaller than the laminar separation region. (4) Turbulent separation was mainly affected by the energy of the boundary layer, and the energy distribution of the boundary layer at the trailing edge of the airfoil was inseparable from the transition position. When the transition position moved back, the flow separation would be reduced. This transition-separation interaction phenomenon of the blunt trailing edge airfoil indicated that a small difference in the transition position could lead to a large change in the overall aerodynamic characteristics. In conclusion, the unique design of the “step” at the lower surface was the main reason of the superiority of DBLN-526 airfoil in unsteady characters. In the blunt trailing edge

airfoil design, controlling the turning point behind cannot only maintain a larger laminar flow area but also reduce separation, so as to achieve the purpose of reducing drag and improving unsteady characteristics.

Mechanistic studies on rounded trailing edge airfoils provide insights into the design of the lower surface of rounded trailing edge airfoils and provide an idea about passive control, which is easy in practical applications. Later, we will study the effect of unsteady inflow conditions and different geometric parameters of the step on the unsteady characteristics of DBLN-526 and will contribute to the design of advanced rounded trailing edge airfoils.

## Data Availability

With the consent of the corresponding author, all data is available.

## Conflicts of Interest

The authors declare that they have no conflicts of interest.

## Acknowledgments

This research was supported by the Natural Science Basic Research Program of Shaanxi Province (No. 2021JQ-076), the Fundamental Research Funds for the Central Universities, and the Foundation of National Key Laboratory of Science and Technology on Aerodynamic Design and Research (No. 6142201200106). All authors are grateful to the professor Lu Xia in northwestern polytechnical university for her help in drawing and writing the paper.

## References

- [1] Y. Ye, R. L. Chen, and P. Li, “Trim investigation for coaxial rigid rotor helicopters using an improved aerodynamic interference model,” *Aerospace Science and Technology*, vol. 85, pp. 293–304, 2019.
- [2] R. Singh, H. Kang, and C. Cameron, “Computational and experimental investigations of coaxial rotor unsteady loads,” in *54th AIAA aerospace sciences meeting, American Institute of Aeronautics and Astronautics*, San Diego, California, USA, 2016.
- [3] M. Potsdam, H. Yeo, and W. Johnson, “Rotor air-loads prediction using loose aerodynamic/structural coupling,” *Journal of Aircraft*, vol. 43, no. 3, pp. 732–742, 2006.
- [4] H. T. Qi, G. Xu, C. Lu, and Y. Shi, “A study of coaxial rotor aerodynamic interaction mechanism in hover with high-efficient trim model,” *Aerospace Science and Technology*, vol. 84, pp. 1116–1130, 2019.
- [5] R. Singh, H. Kang, and J. Sirohi, “Computational investigations of transient loads and blade deformations on coaxial rotor systems,” in *33rd AIAA Applied Aerodynamics Conference*, American Institute of Aeronautics and Astronautics, 2015.
- [6] A. H. Lind and A. R. Jones, “Vortex shedding from airfoils in reverse flow,” *AIAA Journal*, vol. 53, no. 9, pp. 2621–2633, 2015.
- [7] J. Hodara, A. H. Lind, A. R. Jones, and M. J. Smith, “Collaborative investigation of the aerodynamic behavior of airfoils in reverse flow,” *Journal of the American Helicopter Society*, vol. 61, no. 3, pp. 1–5, 2015.

- [8] A. Datta, H. Yeo, and T. R. Norman, "Experimental investigation and fundamental understanding of a full-scale slowed rotor at high advance ratios," *Journal of the American Helicopter Society*, vol. 58, no. 2, pp. 1–17, 2013.
- [9] W. D. Beasley and R. J. Mcghee, *Low-Speed Aerodynamic Characteristics of Airfoil Sections with Rounded Trailing Edges in Forward and Reverse Flow*, NASA-TM-X-3060, 1974.
- [10] B. Ashish, "Aerodynamic design of the X2 technology demonstrator main rotor blade," in *Proceedings of the 64th Annual Forum of the American Helicopter Society*, Montreal, Canada, 2008.
- [11] B. J. Passe, S. Ananth, and D. B. James, "Computational investigation of coaxial rotor interactional aerodynamics in steady forward flight," in *33rd AIAA Applied Aerodynamics Conference*, Dallas, TX, 2015.
- [12] A. H. Lind, J. N. Lefebvre, and A. R. Jones, "Time-averaged aerodynamics of sharp and rounded trailing-edge static airfoils in reverse flow," *AIAA Journal*, vol. 52, pp. 1–18, 2015.
- [13] A. H. Lind, J. N. Lefebvre, and A. R. Jones, "Experimental investigation of reverse flow over sharp and rounded trailing edge airfoils," in *Aiaa Applied Aerodynamics Conference*, San Diego, CA, 2013.
- [14] W. Sun, Z. Gao, Y. Du, and F. Xu, "Mechanism of unconventional aerodynamic characteristics of an elliptic airfoil," *Chinese Journal of Aeronautics*, vol. 28, no. 3, pp. 687–694, 2015.
- [15] L. Zhou, Z. H. Gao, and Y. M. Du, "Flow-dependent DDES/ $\gamma$ - $\overline{Re}_{\theta t}$  coupling model for the simulation of separated transitional flow," *Aerospace Science and Technology*, vol. 87, pp. 389–403, 2019.
- [16] S. Q. Han, W. P. Song, Z. H. Han, S. B. Li, and Y. F. Lin, "Hybrid inverse/optimization design method for rigid coaxial rotor airfoils considering reverse flow," *Aerospace Science and Technology*, vol. 95, article 105488, 2019.
- [17] J. Xu and H. Ma, "Applications of URANS on predicting unsteady turbulent separated flows," *Acta Mechanica Sinica*, vol. 25, no. 3, pp. 319–324, 2009.
- [18] R. B. Langtry and F. R. Menter, "Correlation-based transition modeling for unstructured parallelized computational fluid dynamics codes," *AIAA Journal*, vol. 47, no. 12, pp. 2894–2906, 2009.
- [19] S. L. Krist, R. T. Biedron, and C. L. Rumsey, *CFL3D User's Manual (Var 5.0)*, NASA Langley Research Center, Washington, D.C., 2nd edition, 1998, Report No.: NASA/TM-1998-208444.
- [20] P. R. Spalart and C. L. Rumsey, "Effective inflow conditions for turbulence models in aerodynamic calculations," *AIAA Journal*, vol. 45, no. 10, pp. 2544–2553, 2007.
- [21] D. U. Yiming, G. A. Zhenghong, W. A. Chao, and Q. Huang, "Boundary-layer transition of advanced fighter wings at high-speed cruise conditions," *Chinese Journal of Aeronautics*, vol. 32, no. 4, pp. 799–814, 2019.
- [22] C. H. Sieverding, C. Bagnera, A. C. Boege, J. A. Anton, and V. Luere, "Investigation of the effectiveness of various types of boundary layer transition elements of low Reynolds number turbine bladings," in *ASME Turbo Expo: Power for Land, Sea, and Air*, American Society of Mechanical Engineers Digital Collection, 2004.